3-D Differential SAR Interferometry for Spaceborne SAR Systems with Azimuth Digital Beamforming

Simon Trumpf[a], Pau Prats-Iraola[a], David Tomsu[a], and Alberto Moreira[a]
[a]German Aerospace Center (DLR), Microwaves and Radar Institute, 82234 Wessling, Germany

Abstract

Differential shift estimation is an important task for many applications of synthetic aperture radar (SAR). A new generation of spaceborne SAR systems is being designed to use multiple channels in azimuth, which leads to a large available azimuth bandwidth for processing, allowing for an extension of the nominal interferometric SAR processing to retrieve the differential shift between two acquisitions. This contribution estimates the accuracy of the differential shift retrieval in the along-track direction using a 2-look ScanSAR processing for the particular case of the upcoming ROSE-L mission. The derived performance is then validated with a simulation using extended targets, which shows that the azimuth displacement can be retrieved with sufficient accuracy in order to successfully remove the azimuth phase jumps between bursts occurring in the differential interferogram.

1 Introduction

Modern synthetic aperture radar (SAR) systems aim to maximise the ground coverage by increasing the swath width while maintaining a high resolution in the azimuth direction. In order to combine these two features, advanced SAR techniques, specifically digital beam forming in the form of scan-on receive (SCORE) or multiple azimuth channels (MAPS), are used, as a conventional single-channel Stripmap SAR systems' swath width and azimuth resolution are constrained by the pulse repetition frequency (PRF). While the use of ScanSAR allows to cover a wider swath at the expense of azimuth resolution, the usage of multi-channel sensors allows to improve the azimuth resolution w.r.t. a conventional system. One example for a mission that uses ScanSAR in combination with multiple channels in azimuth is ROSE-L, which in addition applies SCORE at each sub-swath to improve the signal-to-noise (SNR) ratio. ROSE-L is a L-band SAR mission in the frame of the Copernicus Sentinel expansion Programme of the European Union and the European Space Agency, employing a planar antenna with five receive apertures and ScanSAR as standard acquisition mode [1, 2]. For ROSE-L, the available azimuth bandwidth after the MAPS reconstruction exceeds the required processing bandwidth by roughly a factor of two. This contribution evaluates an extended processing approach which uses the otherwise unused bandwidth in order to retrieve the along-track and across-track components of the ground deformation separately. Extending the processed bandwidth allows to use a 2-look ScanSAR approach, which has already been used in [3, 4] to retrieve the azimuthal component of the displacement and proposed for the ROSE-L mission in [5]. Thus, it is well suited for the retrieval technique analysed in this contribution. The proposed deformation retrieval would allow to enhance the observation of deformations due to earthquakes or volcanic activities, one of the many applications that SAR interferometry is already successfully used for [6]. This contribution puts its focus on the processing scheme to retrieve the 2-D deformation signals as well as on the expected accuracy of the along-track deformation retrieval, which is limited by the ROSE-L antenna pattern shown in Fig. 1. The limitation occurs because of the decreasing gain beyond the 1-look processing bandwidth, hence leading to a decreased retrieval accuracy due to the increase of the azimuth ambiguities and noise level in these areas.

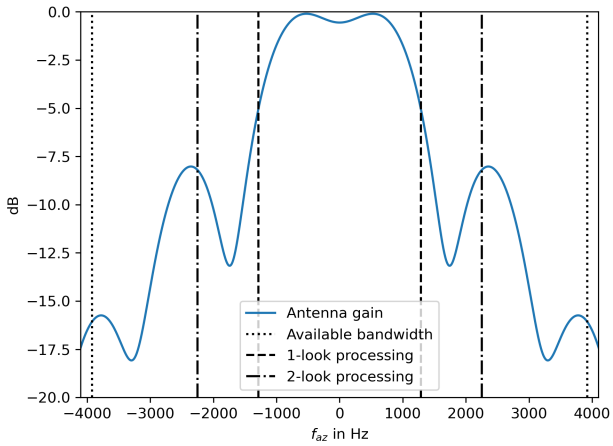

Figure 1 Two-way antenna pattern of the ROSE-L satellite in azimuth dimension. The dotted lines enclose the available bandwidth after the MAPS reconstruction, the dashed lines the bandwidth used for the nominal 1-look processing approach and the dash-dotted lines the bandwidth of the 2-look ScanSAR approach used in this contribution.

This contribution is structured as follows. Section 2 explains the structure of the deformation retrieval chain. Sec-

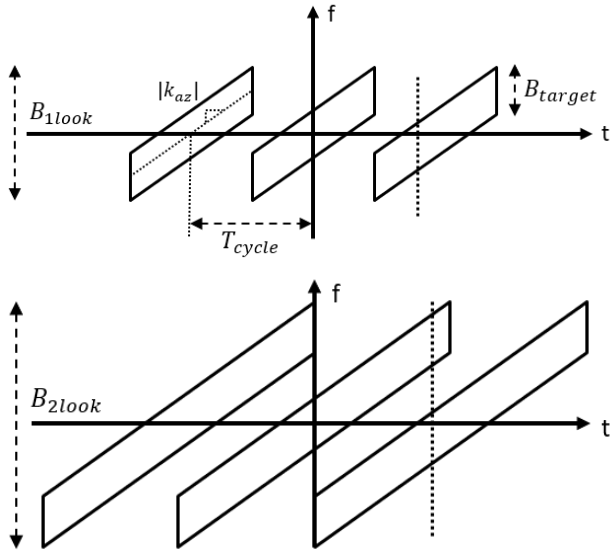

Figure 2 Time-frequency diagrams of 1-look and 2-look ScanSAR. Top panel: 1-look ScanSAR, the exemplary point marked with the dotted line in the right burst is covered once. Bottom panel: 2-look ScanSAR, the same point is covered twice.

tion 3 presents an analytic performance estimation for the azimuth deformation using the 2-look approach, while Section 4 shows the structure of the implemented simulations and presents their results. Finally, conclusions are drawn and an outlook is provided in Section 5.

2 2-Look ScanSAR

In SAR systems with multiple receive apertures like ROSE-L, the acquired data for all N_{ch} channels have to be reconstructed in order to obtain an unaliased SAR image. Digital processing algorithms as described in [7] are used, such that after the reconstruction step a signal with bandwidth

$$B_{\text{rec}} = N_{ch} \cdot \text{PRF} \tag{1}$$

is obtained. In ScanSAR, the temporal extent of each focused burst $T_{\text{burst,foc}}$ is related to the focusing bandwidth B_{foc}, the azimuth Doppler rate k_{az} and the ScanSAR burst duration $T_{\text{burst,raw}}$ or the bandwidth of a target B_{target} as

$$\begin{aligned} T_{\text{burst,foc}} &= B_{\text{foc}}/|k_{az}| - T_{\text{burst,raw}} \\ &= (B_{\text{foc}} - B_{\text{target}})/|k_{az}|. \end{aligned} \tag{2}$$

In order to have a continuous coverage for all sub-swaths, $T_{\text{burst,foc}}$ is set to the ScanSAR cycle time T_{cycle}, resulting in a minimal 1-look bandwidth B_{1look} of

$$B_{\text{1look}} = |k_{az}| \cdot T_{\text{cycle}} + B_{\text{target}}, \tag{3}$$

which corresponds to the scenario shown in the upper panel in Fig. 2. According to (2), every target on ground can be covered by more than one burst by enhancing the processed bandwidth. The particular case shown in the lower time-frequency diagram in Fig. 2, where every target is covered

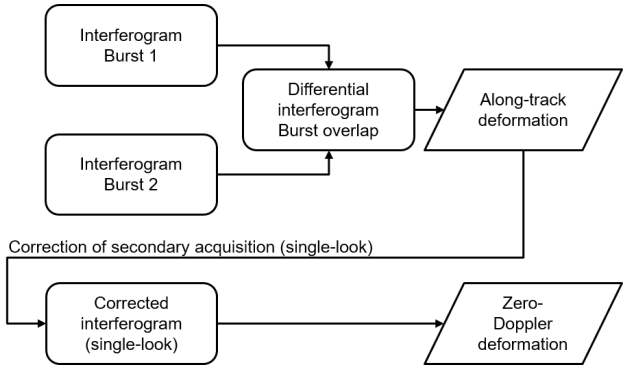

Figure 3 The simplified processing chain to retrieve values of the deformation in azimuth and zero-Doppler direction.

by two different bursts is referred to as 2-look ScanSAR. Due to the approximate linear relation between time and frequency, the minimal required bandwidth for processing results to

$$B_{\text{2look}} = 2 \cdot |k_{az}| \cdot T_{\text{cycle}} + B_{\text{target}}. \tag{4}$$

Fig. 2 also shows that the two looks occupy different parts of the spectrum, leading to different Doppler centroid frequencies. The separation of these two Doppler centroids can be computed as

$$\Delta f = |k_{az}| \cdot T_{\text{cycle}}. \tag{5}$$

This spectral diversity is equivalent to different look angles, and can be used to compute the relative shift in azimuth between two acquisitions, as shown in [8, 3]. During the interferometric processing, the retrieved azimuth shift can be used to correct the 1-look interferogram to obtain the deformation in zero-Doppler direction. As a result, the processing provides two different deformation values for each radar pixel: A value for the azimuthal component of the deformation and a value for the zero-Doppler component of the deformation, i.e., the 2-D deformation in radar coordinates is retrieved. A scheme of the described processing chain is shown in Fig. 3.

By combining ascending and descending passes it is then possible to compute the 3-D deformation (easting, northing and vertical), e.g., by means of a conventional weighted least squares inversion. One shall consider that the measurement in the azimuth direction will have in general a worse performance, as indicated in the next section. Our suggestion is to try to achieve a similar accuracy as the line-of-sight measurement by using more looks when estimating the azimuth shift.

3 Performance Analysis

For conventional SAR acquisitions, the optimal estimator for the azimuth shift is the cross-correlation operation. Its Cramér-Rao bound is given by [9]

$$\sigma_{CC,CR} = \sqrt{\frac{3}{2N_{\text{looks}}}} \frac{\sqrt{1-\gamma^2}}{\pi\gamma} \frac{v_g}{B_{\text{target}}}, \tag{6}$$

where N_{looks} is the number of looks, γ the interferometric coherence, v_g the platform velocity over ground and B_{target} the bandwidth of a target in azimuth. Note that the performance is limited by the azimuth resolution. The standard deviation of the 2-look ScanSAR case can be derived equivalently to the one of the split-bandwidth case shown in [9]. While for the split-bandwidth case a similar coherence can be assumed for both looks, this assumption does not hold here due to the significantly lower antenna gain on the edges of the 2-look bandwidth. The two looks are thus considered separately and the resulting variance of the 2-look measurement σ^2_{2LSC} is computed as

$$\sigma^2_{\text{2LSC}} = \sigma^2_{L1} + \sigma^2_{L2}. \tag{7}$$

The standard deviation for each look follows the equation similar to the split-bandwidth case

$$\sigma_{L\{1,2\}} = \frac{1}{\sqrt{2N_{\text{looks}}}} \frac{\sqrt{1-\gamma^2_{L\{1,2\}}}}{\gamma_{L\{1,2\}}} \frac{v_g}{2\pi\Delta f}, \tag{8}$$

which results in a two-look measurement accuracy with

$$\sigma_{\text{2LSC}} = \frac{1}{\sqrt{2N_{\text{looks}}}} \sqrt{\left(\frac{1-\gamma^2_{L1}}{\gamma^2_{L1}} + \frac{1-\gamma^2_{L2}}{\gamma^2_{L2}}\right)} \frac{v_g}{2\pi\Delta f}. \tag{9}$$

To determine the interferometric coherence of the looks, several factors have to be considered. Temporal changes, thermal noise and azimuth ambiguities cause decorrelation, which deteriorate the signal quality, leading to worse estimates of the deformation. This is especially relevant here due to the decreasing gain of the antenna pattern in azimuth towards the edges of the 2-look ScanSAR bandwidth, resulting in an increase of noise and azimuth ambiguities. The decorrelation due to the signal-to-noise ratio γ_{SNR} and due to the azimuth-ambiguity-to-signal ratio γ_{AASR} are thus relevant measures for the performance analysis. Together with temporal decorrelation γ_{temp}, the coherence model assumed for each look follows the equation of the well known form

$$\gamma_{L\{1,2\}} = \gamma_{\text{temp}} \cdot \gamma_{\text{SNR}\{1,2\}} \cdot \gamma_{\text{AASR}\{1,2\}} \tag{10}$$

where the subscript $\{1,2\}$ refers to the indices of the respective looks.

3.1 Decorrelation Due to Noise

With the assumption of white noise, the SNR depends on the power of the returned radar signal and the induced noise power. Given the normalised radar backscatter coefficient in slant range β_0, the antenna gain G and the noise equivalent beta nought (NEBN), the SNR can be computed as

$$\text{SNR} = \frac{\beta_0 \cdot G}{\text{NEBN}}. \tag{11}$$

Assuming a similar SNR in primary and secondary acquisition for each of the looks, the coherence is then computed as [10]

$$\gamma_{\text{SNR}\{1,2\}} = \frac{1}{1 + \text{SNR}^{-1}_{\{1,2\}}}. \tag{12}$$

Table 1 Simulation parameters for ROSE-L.

Parameter	Value
N_{ch}	5
PRF_{ch}	$1567.85\,\text{Hz}$
v_{eff}	$7142.76\,\text{m}\,\text{s}^{-1}$
NEBN	$-26.2\,\text{dB}$
N_{looks}	50
B_{target}	$640\,\text{Hz}$
γ_{temp}	0.7

3.2 Decorrelation Due to Azimuth Ambiguities

Azimuth ambiguities may cause additional decorrelation as the signal power decreases towards the burst edges while the power of the ambiguities might not. Similar to the noise, the AASR is assumed the same for primary and secondary acquisitions of the same look. It has to take into account the azimuth reconstruction due to the multi-channel nature of the system and is computed as [7]

$$\text{AASR}_{\{1,2\}} = \frac{p_{a\{1,2\}}}{p_{s\{1,2\}}} \tag{13}$$

where $p_{s\{1,2\}}$ and $p_{a\{1,2\}}$ are the total power contributions of the focused signal and its ambiguities for each look, respectively. The coherence follows as [11]

$$\gamma_{\text{AASR}\{1,2\}} = \frac{1}{1 + \text{AASR}_{\{1,2\}}}. \tag{14}$$

Note that the model above assumes decorrelated ambiguities, which might not be necessarily the case, especially for SAR missions with a small orbital tube. In such cases, coherent azimuth ambiguities can result in interferometric biases in scenes with very heterogeneous backscattering [12].

3.3 Application to the ROSE-L Case

In the case of ROSE-L the accuracy is computed using the antenna pattern shown in Fig. 1 and the parameters listed in Table 1. The results shown in the following consider the case of a target located at burst centre, where the looks with Doppler centroids $f_{DC} = 0\,\text{Hz}$ and $f_{DC} = \Delta f = 1930\,\text{Hz}$ are exploited and thus the quality of the looks varies the most. However, the same analysis can be done for a target at a 1-look burst edge with parameters adapted accordingly. The SNR values are computed from radar backscatter coefficient, NEBN and the antenna gain at the respective Doppler centroids. Some exemplary values for a backscatter coefficient $\beta_0 = -11\,\text{dB}$ are listed in Table 2. Just like the SNR, the AASR for ROSE-L varies depending on the Doppler centroid of the target. It is computed by adding all the ambiguous contributions and dividing it by the main signal power (see (13)). Hereby the MAPS reconstruction has to be considered, which reconstructs the signal in $N_{ch} = 5$ different intervals with scaled ambiguous contributions. The resulting AASR after focusing is shown in Fig. 4. The resulting retrieval accuracy is shown

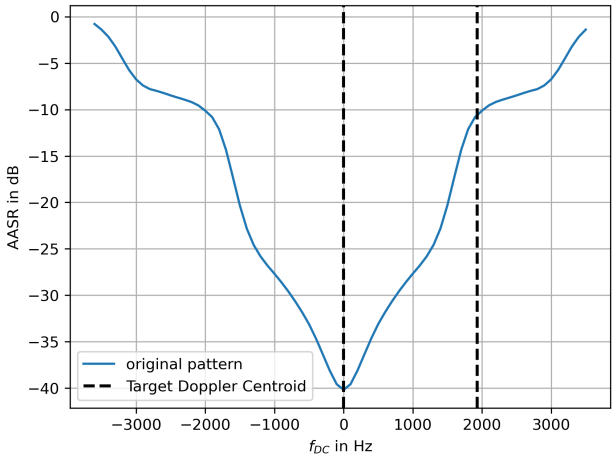

Figure 4 AASR of ROSE-L computed from the antenna pattern after application of the azimuth reconstruction algorithm and focusing. For the analysed 2-look ScanSAR mode, a point in the burst centre will be covered by the neighbouring burst with a Doppler centroid at approximately $f_{DC} = 1930\,\text{Hz}$ (vertical dashed line on the right).

Table 2 Reference values for a target at burst centre with $\beta_0 = -11\,\text{dB}$.

Look 1, $f_{DC} = 0\,\text{Hz}$	
Parameter	Value
SNR	15.2 dB
γ_{SNR1}	0.97
AASR	−40.2 dB
γ_{AASR1}	0.99
γ_{L1}	0.68
Look 2, $f_{DC} = 1930\,\text{Hz}$	
Parameter	Value
SNR	4.2 dB
γ_{SNR2}	0.72
AASR	−10.8 dB
γ_{AASR2}	0.92
γ_{L2}	0.47

in Fig. 5. An accuracy of less than 10 cm can be achieved for backscatter values $\beta_0 \geq -10\,\text{dB}$ approximately. This is a significant improvement of a factor 4-6 compared to the cross-correlation case, which is limited by the azimuth resolution. The given multilooking of $N_{\text{looks}} = 50$ corresponds to a resolution of $50\,\text{m} \times 50\,\text{m}$ in azimuth and range, however note that the variance of the deformation measurement can still be decreased by increasing N_{looks}, as becomes clear when looking at (9).

4 Experimental Validation

To verify the analytic results, a more realistic simulation of the previously described algorithm is implemented. The following subsections explain the structure of the implemented simulation and its results.

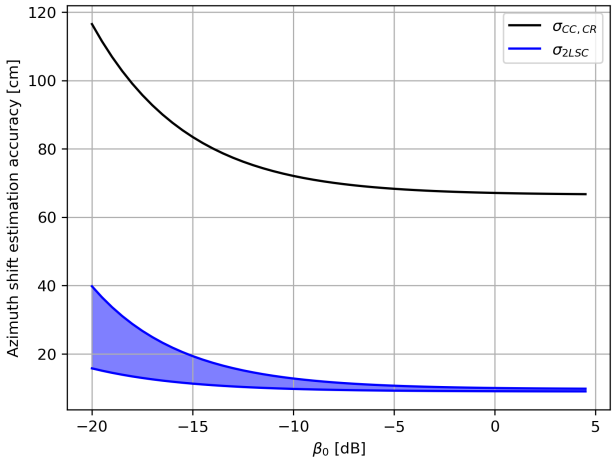

Figure 5 Azimuth shift estimation accuracies over backscatter coefficient. 1-look Cramér-Rao bound is in black and 2-look worst case and best case are in blue. Table 2 lists examplary values of the worst case.

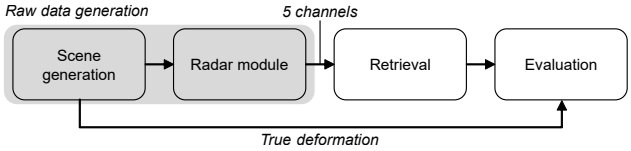

Figure 6 Structure of the simulation with the four modules for scene generation, radar signal generation, retrieval and evaluation.

4.1 Implementation

The simulation consists of the four main steps shown in Fig. 6. The scene generation module creates a pair of artificial SAR images of a scene that is subject to a known deformation, using an artificial 3-D deformation generated from the Okada model [13] and a real backscattering SAR image, in this case of Sentinel-1. The data are then upsampled in azimuth to a sampling frequency $\text{asf} = 15 \cdot \text{PRF}_{ch}$, where PRF_{ch} is the PRF of one channel. The radar module generates raw SAR data by defocusing the images by applying an azimuth decompression, and then accounting for the used multi-channel ScanSAR acquisition mode. In order to account for the MAPS, the acquired signals for each of the channels are derived by multiplying the oversampled signal with the residual bistatic channel impulse responses $H_j(f)$ [7] for each channel j given by

$$H_j(f) = \exp\left(-j \cdot \frac{\pi \cdot \Delta x_j^2}{2\lambda \cdot R_0}\right) \cdot \exp\left(-j \frac{\pi \cdot \Delta x_j}{v_{\text{eff}}} \cdot f\right), \tag{15}$$

where Δx_j is the distance of the j-th receive aperture's phase centre to the transmit aperture's phase centre, λ is the carrier frequency's wavelength and R_0 is the minimal slant range distance. Then azimuth ambiguities are introduced by subsampling the raw data in time domain to an azimuth sampling frequency $\text{asf} = \text{PRF}_{ch}$, which adds 14 ambiguities, four of which are later compensated for by the azimuth reconstruction algorithm. As an additional source

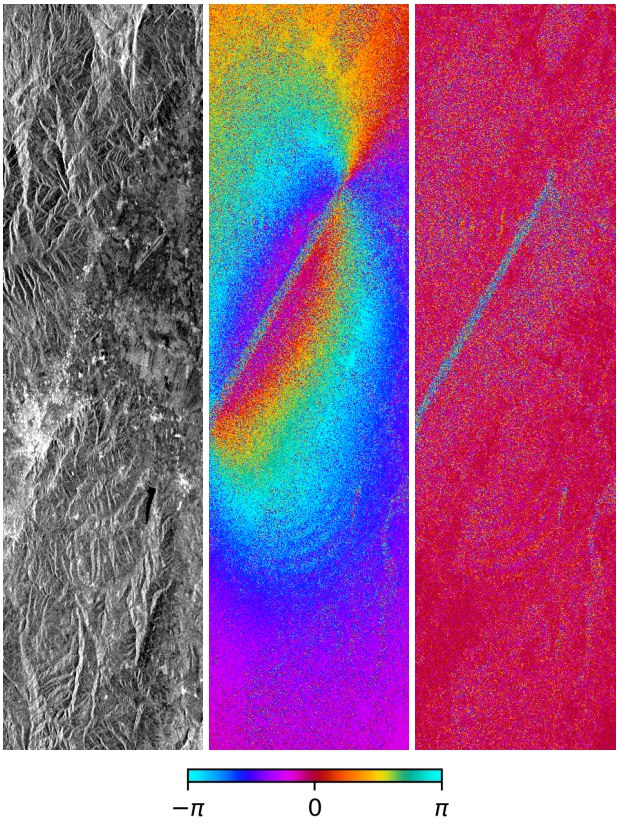

Figure 7 Left: Reflectivity of the Sentinel-1 image used for the simulation including the Turkish city of Antakya. Centre: Phase of the differential 2-look interferogram, the phase contribution due to the along-track deformation is clearly visible. Right: Difference of the retrieved 2-look interferometric phase and the phase due to the along-track deformation used for the scene generation. Azimuth is vertical. The figure shows a cutout of the simulated scene.

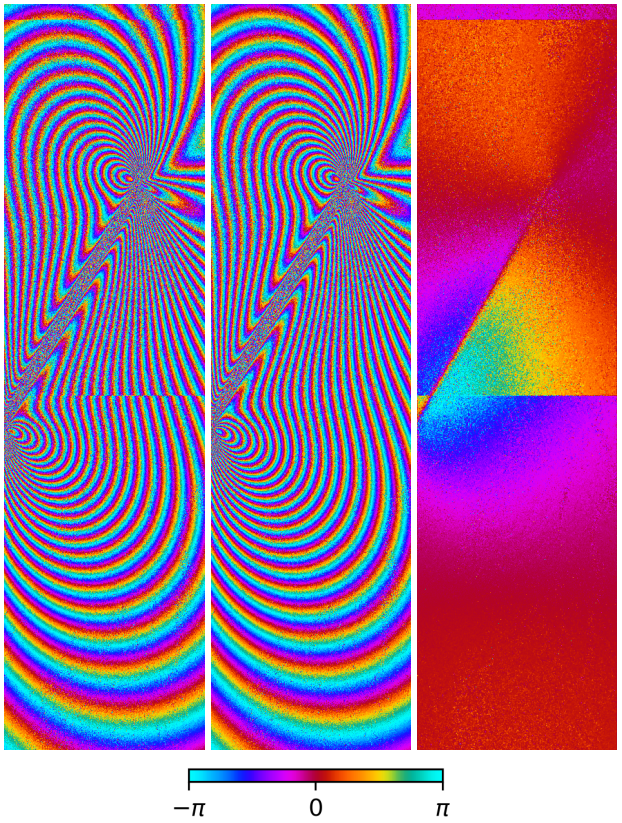

Figure 8 Left: 1-look interferogram in line of sight, phase jumps can be observed at the burst edges. Centre: 1-look interferogram after removal of along-track deformation estimated by 2-look processing, where no phase jumps between bursts can be observed. Right: Along-track component of the interferometric phase in line of sight. Azimuth is vertical. The figure shows a cutout of the simulated scene.

of decorrelation, independent realisations of circular white Gaussian noise are added to the channel signals. The injected noise power is hereby equivalent to the NEBN. Finally, the ScanSAR acquisitions are retrieved by cutting bursts from the raw data. The retrieval module computes the reconstructed and focused signal for both acquisitions and implements the interferometric processing described in Section 2. Hereby the signal is focused with the 2-look bandwidth B_{2look} given in (4) for the along-track deformation retrieval, but limited to the 1-look bandwidth B_{1look} from (3) for the computation of the interferogram in line of sight.

4.2 Results

For a simulation using the parameters from Table 1 the different interferometric results are shown in Fig. 7 and Fig. 8. The results of the 2-look processing are shown in Fig. 7 along with the Sentinel-1 reflectivity used in the simulation, corresponding to a data take over the Turkish-Syrian border close to the East Anatolian Fault. Note that instead of the temporal coherence given in the table, the actual coherence of the Sentinel-1 acquisition has been used for the simulation. As these data are acquired in C-band, a higher dynamic range of the reflectivity and a higher coherence would be expected for a similar acquisition in L-band [14]. Fig. 8 shows the results of the 1-look processing. It can be clearly observed that the phase jumps that occur due to the along-track motion of the scene can be properly compensated for with the proposed processing approach.

To analyse the retrieval accuracy in different parts of the bursts, a simulation with clutter as signal is more suited than the Sentinel-1 reflectivity from the previous results. The standard deviation of the measured deformation error in along-track direction along azimuth for clutter with $\beta_0 = -11\,\text{dB}$ is shown in Fig. 9. The deformation can be retrieved with an accuracy of $9\,\text{cm}$ to $15\,\text{cm}$. As expected, the accuracy depends on the position of the target within the burst, while best case and worst case accuracies are in the order of magnitude predicted by the analytic approach. Possible deviations between simulation and analysis can be explained by the role of coherent ambiguities, which are not considered in the analytic approach but occur in the simulation.

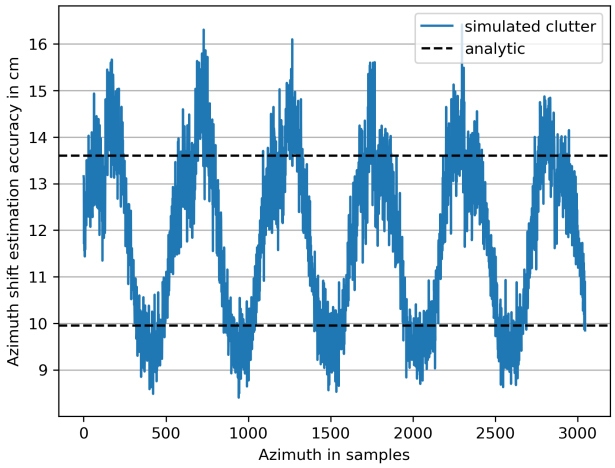

Figure 9 Error standard deviation of the measured along-track deformation along azimuth for a simulated clutter signal (blue) and the corresponding analytic values (black). The error is inhomogeneous due to the different signal qualities in different parts of the bursts.

5 Conclusion and future work

This contribution has shown that the current system design of the ROSE-L system allows for measurements of the along-track deformation using a 2-look ScanSAR approach, which allows a retrieval accuracy beyond the performance that can be obtained with the azimuth resolution. The advantage is that nothing needs to be changed in the system, being the only requirement that the ground processor focuses a wider azimuth bandwidth. The exact accuracy hereby depends on the multilooking. For example, with a resolution of $50\,\mathrm{m} \times 50\,\mathrm{m}$ in azimuth and ground range respectively a mean accuracy of approximately $12\,\mathrm{cm}$ can be achieved for a region with a mean power of $-11\,\mathrm{dB}$. The proposed processing also allows the independent retrieval of the along-track and across-track deformations, such that by combining ascending and descending orbits one can retrieve a 3-D deformation map.
While the accuracy within the current system depends on the target position within the overlapped bursts, the difference in performance are not significant. Further simulations (not shown) have been performed by using an alternative antenna pattern, as suggested in [5]. In this case, variability of the retrieval accuracy within the burst is reduced while maintaining the same mean accuracy. This comes at the price of a reduced peak antenna gain and thus a worse SNR and AASR within the 1-look bandwidth. Additional investigations with alternative transmit or receive antenna patterns would be needed to evaluate whether the impact on the 1-look images could be minimized.

6 Literature

[1] D. Geudtner et al., "Copernicus ROSE-L SAR mission," EUSAR, 14th European Conference on Synthetic Aperture Radar, Leipzig, Germany, 2022, pp. 1-4.

[2] M. Zimmermanns and C. Roemer, "Copernicus HPCM: ROSE-L SAR instrument and performance overview," EUSAR, 14th European Conference on Synthetic Aperture Radar, Leipzig, Germany, 2022, pp. 1-6.

[3] P. Prats-Iraola et. al., "Repeat-pass interferometric experiments with the TanDEM-X constellation for accurate along-track motion estimation," IGARSS, IEEE International Geoscience and Remote Sensing Symposium, Milan, Italy, 2015, pp. 4077-4080.

[4] N. Yague-Martinez, P. Prats-Iraola, T. Kraus, S. Wollstadt and R. Scheiber, "Experimental validation with TerraSAR-X/TanDEM-X of advanced interferometric modes for accurate retrieval of azimuthal displacements," IGARSS, IEEE International Geoscience and Remote Sensing Symposium, Beijing, China, 2016, pp. 1444-1447.

[5] S. Perna, F. Longo, S. Zoffoli, M. Davidson, L. Iannini and R. Lanari, "A Conceptual Performance Study on a Two-Look ScanSAR Mode Configuration for the Forthcoming ROSE-L Mission," IEEE Transactions on Geoscience and Remote Sensing 62, 2024, pp. 1-18.

[6] J. Biggs and T. J. Wright, "How satellite InSAR has grown from opportunistic science to routine monitoring over the last decade," Nature Communications 11.1, 2020.

[7] N. Gebert, G. Krieger and A. Moreira, "Digital beamforming on receive: Techniques and optimization strategies for high-resolution wide-swath SAR imaging," IEEE Transactions on Aerospace and Electronic Systems 45.2, 2009, pp. 564-592.

[8] R. Scheiber and A. Moreira, "Coregistration of interferometric SAR images using spectral diversity," IEEE Transactions on Geoscience and Remote Sensing 38.5, 2000, pp. 2179-2191.

[9] R. Bamler and M. Eineder, "Accuracy of differential shift estimation by correlation and split-bandwidth interferometry for wideband and delta-k SAR systems," IEEE Geoscience and Remote Sensing Letters 2.2, 2005, pp. 151-155.

[10] D. Just and R. Bamler, "Phase statistics of interferograms with applications to synthetic aperture radar," Applied optics 33.20, 1994, pp. 4361-4368.

[11] G. Krieger et al., "The TanDEM-X mission: A satellite formation for high-resolution SAR interferometry," European Radar Conference, Munich, Germany, 2007, pp. 83-86.

[12] M. Villano et. al., "Impact of azimuth ambiguities on interferometric performance," IEEE Geoscience and Remote Sensing Letters 9.5, 2012, pp. 896-900.

[13] Y. Okada, "Surface deformation due to shear and tensile faults in a half-space," Bulletin of the seismological society of America 75.4 , 1985, pp. 1135-1154.

[14] A. Parizzi, X. Cong and M. Eineder, "First Results from Multifrequency Interferometry. A comparison of different decorrelation time constants at L, C, and X Band," ESA FRINGE Workshop 2009, Frascati, Italy, ESA Scientific Publications (SP-677), pp. 1-5.